

Highlights

A Parametric Study on the Pulsation of Burner-Stabilized CH₄-O₂ Flames Moderated by CO₂ Addition – Frequencies, Modes and Regime Diagrams

Xiangyu Nie, Shuoxun Zhang, Shengkai Wang*

- Novelty and Significance

This work presents, to the authors' knowledge, the first systematic measurements of pulsating flame instabilities in burner-stabilized premixed methane-oxygen flames across a wide range of experimental conditions (equivalence ratios, dilution factors and flow rates). The combination of a porous-plug burner and oxygen-enriched combustion amplifies weak phenomena that commonly occur under extreme conditions of very high Lewis number, making them observable under moderate conditions that are easily accessible in a laboratory. Additionally, this work reports direct measurements of the spatiotemporal evolution of flame chemiluminescence and gas temperature during pulsation cycles. Based on phase-locked analysis of the data, this study has revealed an interesting mode-transition phenomenon of the flame pulsation. The results of this work should prove useful for both fundamental research on flame dynamics and practical applications of CO₂-moderated oxy-combustion.

- Author Contributions

Xiangyu Nie: Data curation, Investigation, Writing - original draft.
Shuoxun Zhang: Data curation, Investigation, Writing - original draft.
Shengkai Wang: Conceptualization, Formal Analysis, Funding acquisition, Methodology, Supervision, Writing — original draft, Writing - review & editing.

A Parametric Study on the Pulsation of Burner-Stabilized CH₄-O₂ Flames Moderated by CO₂ Addition – Frequencies, Modes and Regime Diagrams

Xiangyu Nie, Shuoxun Zhang, Shengkai Wang*

^aSKLTCS, CAPT, School of Mechanics and Engineering Science, Peking University, 5 Yiheyuan Road, Haidian District, Beijing, 100871, China

Abstract

This study investigated the pulsating instability of burner-stabilized premixed CH₄-O₂ flames at various levels of CO₂ dilution. Experiments were conducted using a water-cooled porous-plug burner of 18 mm diameter over a wide range of mixture compositions and flow rates, during which time-resolved measurements of flame chemiluminescence and gas temperature were obtained. The primary oscillation frequencies of the pulsating flames were determined using fast Fourier transform and harmonic power analysis. Phase-locked analysis of the chemiluminescence images revealed an interesting mode-transition phenomenon of the flame oscillations. Under fuel-rich conditions with relatively low heat release rates and low flow rates, the flames exhibited quasi-periodic single-mode oscillations. These oscillations were modulated by low-frequency flame flickering instabilities at elevated flow rates, which created sidebands around the primary oscillation frequency. At higher heat release rates, the flickering instability further triggered mode splitting, eventually leading to multi-mode oscillations. Regime diagrams of the flame oscillation modes, as well as the stability boundaries, were obtained under various fuel flow rates. These findings can be useful for both fundamental research on flame dynamics and practical applications of CO₂-moderated oxy-combustion.

Keywords: Pulsating Instability; Oxy-Combustion; Porous-Plug Burner; Chemiluminescence; Laser Absorption Spectroscopy; Phase-Locked Analysis

1. Introduction

Combustion instabilities, caused either by the interaction of reacting flow with combustor components or by intrinsic processes related to flame dynamics, pose critical challenges to the modern design of power generation and propulsion systems aimed at achieving cleaner and more efficient operations at higher safety levels [1, 2, 3], especially amid the increasing adoption of renewable fuels [4] and carbon-neutral combustion strategies [5]. For example, fuels obtained from renewable sources typically contain a significant portion of lightweight molecules that exhibit kinetic, thermodynamic, and transport properties drastically different from those of conventional large hydrocarbon fossil fuels. These properties can lead to intrinsic flame instabilities within the combustion process itself, even in the absence of surrounding components [6].

An important type of such instability is the thermo-diffusive instability that arises from the imbalance between heat and mass transfer [7, 8, 9]. Depending on the effective Lewis number (Le) of the reactive mixture, the flame can exhibit either spatial cellular structures (at $Le < 1$) or temporal pulsation of the reaction front (at $Le > 1$). Although the former has been extensively investigated, especially in lean combustion systems of lightweight fuels such as hydrogen and methane [10, 11, 12, 13, 14, 15, 16, 17, 18], experimental studies on the latter remain relatively scarce.

From a physics perspective, this scarcity is likely due to the criterion for the onset of pulsating instabilities that rendered experimental observation difficult. According to the classic theoretical analysis of Sivashinsky [19], pulsating instability in a freely propagating premixed flame can occur only when $Ze(Le - 1) > 4(1 + \sqrt{3})$, where Ze is the Zeldovich number representing the non-dimensional overall activation energy of the mixture. This requires the Lewis number to be impractically high for most fuel-air mixtures [20], except for very rich hydrogen/air mixtures [21]. Though not being an issue for theoretical and computational studies [22, 23], where arbitrarily large Lewis numbers can be accessed [24, 25, 26], it has posed substantial challenge for general experimental measurements of pulsating instability in freely propagating flames.

In light of this challenge, researchers have resorted to alternative platforms, such as the porous-plug burner, for the experimental investigation of flame pulsation dynamics (for example, see [27, 28]). This type of burner features a flat surface made of porous metal plug, which generates a uni-

form velocity profile and also acts as a heat sink that helps to anchor the flame. The presence of a porous plug amplifies the flame instability through interactions with the boundary conditions of the burner, thereby making the pulsation phenomena observable over a wider range of conditions [29], especially at much lower Lewis numbers that are more relevant to practical engines and combustors. Furthermore, from a pragmatic perspective, this configuration perhaps better represents realistic situations, as all practical combustors have boundaries.

Some pioneering investigations on the thermo-diffusive pulsation of burner-stabilized flames date back to the 1980s and 1990s. For example, Blackshear et al. [30] observed flame front oscillations in experiments with lean propane and rich methane–air mixtures; Pearlman and Ronney [31] studied a variety of pulsation modes (including concentric rings and rotating spiral waves) in methane, propane, and butane flames in air. Recently, there has been a proliferation of new experimental and computational studies in this area (for example, see [21, 32, 20, 33, 34, 35, 36]), focusing primarily on methane-air and hydrogen-air flames. However, for flames with enriched or pure oxygen as the oxidizer, a comprehensive characterization of the pulsating instability remains lacking. These flames are expected to exhibit substantially different instability boundaries and oscillation behaviors due to their higher volumetric heat release rates.

Extended study on this topic is important not only for advancing fundamental flame dynamics research but also for practical applications of oxy-fuel combustion. One prominent application is in rocket engines powered by liquid oxygen and hydrocarbon fuels [37]. The successful operation of advanced rocket thrust chambers demands robust mitigation of combustion instabilities, particularly inside the gas generator, where combustion of the methane-oxygen mixture occurs at fuel-rich conditions and can be subject to thermo-diffusive pulsation [38]. Aside from propulsion applications, oxy-combustion is also receiving increased attention in power generation as a promising decarbonization strategy that simplifies CO₂ capture by eliminating nitrogen from the exhaust stream [39, 40]. In such systems, flue gas recirculation is often required to moderate flame temperature [41, 42], making it essential to account for the effects of CO₂ dilution as well. However, as previous studies have suggested [5, 43], the flame instability characteristics of O₂/CO₂ combustion systems are quite different from combustion in air, because (a) the oxygen enrichment modifies the Zeldovich number by changing the effective active energy and raising the adiabatic flame temperature,

and (b) the introduction of CO_2 molecules in the unburnt gas mixture modifies its effective Lewis number. These instability characteristics merit further investigation.

The current study aims to extend previous knowledge on pulsating flame instability by systematically exploring the stability boundary, dominant frequency, and modal characteristics of this instability under conditions of oxy-combustion and more realistic thermal boundaries with finite heat loss. The rest of this paper is organized as follows: Section 2 elaborates on the methods of experimental measurement and data analysis; Section 3 presents the measurement results and discusses the frequencies, modes, and regime diagrams of the observed flame oscillation phenomena; and Section 4 provides the concluding remarks.

2. Methods

2.1. Experimental method

The current flame experiments were conducted on a custom-built McKenna-type burner, as shown in Fig. 1. The burner had a circular sintered bronze plug of 18 mm diameter that was water-cooled to maintain a stable temperature. The temperature of the porous plug was continuously monitored using an embedded K-type thermocouple (Omega TJJ36-CAXL-020-12). High-purity CH_4 (99.99%-grade), O_2 (99.999%-grade), and CO_2 (99.999%-grade) were supplied to the bottom of the burner, where they were thoroughly mixed by an in-line static mixer before passing through the porous plug. The flow rates of fuel, O_2 , and CO_2 were precisely controlled by three Alicat MC series mass flow controllers, with typical uncertainties of 0.1%, 0.2%, and 0.5%, respectively.

Multiple diagnostic methods were employed to investigate the flame oscillation dynamics, including: (1) a spatially and spectrally modulated multi-color laser absorption system for spatiotemporally resolved measurements of gas temperature and CO_2 mole fraction; (2) an image-intensified high-speed camera for spatiotemporally resolved imaging of the line-of-sight integrated OH^* chemiluminescence (as a proxy for the local heat release rate); and (3) a photomultiplier tube (PMT) for microsecond-resolved measurements of global chemiluminescence variations and transient phenomena.

The current laser absorption diagnostic used two distributed-feedback interband-cascade lasers (Nanoplus) to probe 12 absorption features of hot

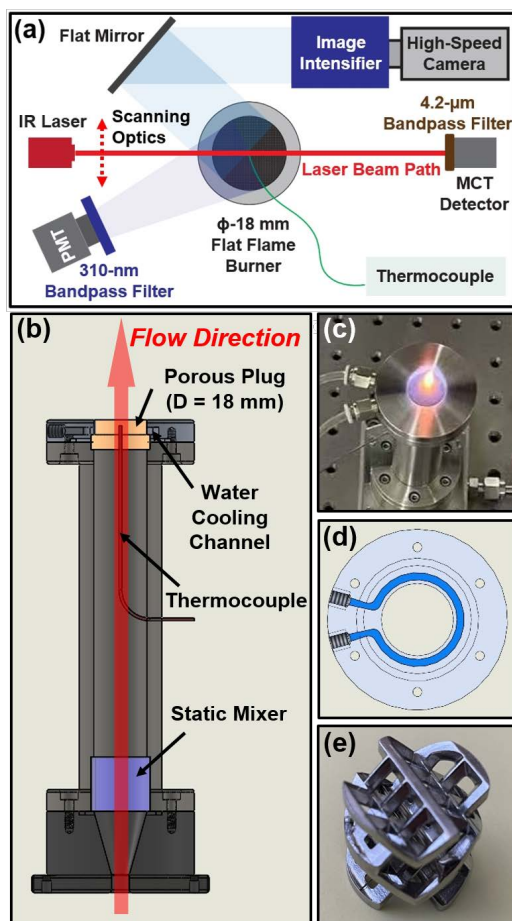


Figure 1: The current experimental setup: (a) schematic of the overall diagnostic system and burner; (b) detailed configuration of the porous-plug burner; (c) example of a burner-stabilized flame; (d) detailed view of the water cooling channel; (e) photograph of the static mixer.

CO₂ molecules near the ν_3 bandhead at a scan rate of 10 kHz. These transitions have drastically different temperature sensitivities. From the relative intensities of these transitions, the gas temperatures were determined with high sensitivity and robustness. Spatially resolved measurements were enabled by a 2D high-speed parallel beam scanning system consisting of a 2D galvo scanner (Thorlabs, GVS102 2D) and a pair of off-axis parabolic mirrors placed upstream and downstream of the measurement region. The galvo scanner was located at the focus of the upstream off-axis parabolic

mirror, ensuring that the reflected beams remained parallel to its axis. The downstream mirror focused the parallel beams on a photodetector that was bandpass-filtered to block the background infrared emission of the flames. A planar measurement speed of 200 Hz was routinely achieved. Further details of this diagnostic method have been documented in a separate work of the authors [44] and are omitted here for brevity.

Time-synchronized measurements of flame chemiluminescence were conducted using an image-intensified high-speed monochromatic camera (Phantom v611) at a frame rate of 10 kHz and a bit depth of 12 bits. To avoid saturation effects, the gain of the image intensifier (Intelligent Scientific Systems, Model EyeiTS) was adjusted to yield a maximum pixel value of approximately 75% of the camera's full range. For top-view measurements of the flames, a flat mirror was placed 20 cm above the burner. This imaging setup provided a depth of field of approximately 6 mm, effectively restricting the recorded emission to a narrow region surrounding the flame front while blurring the out-of-focus signal from further downstream. This allowed for selective visualization of the reaction zone and minimized interference from background emission. Further details of the imaging setup were documented in a previous study by the authors [45]. The flames were recorded at a pixel resolution of 256 x 256 and a physical resolution of 0.11 mm x 0.11 mm per pixel. During each measurement, a sequence of 10,000 consecutive images was recorded.

Side-view measurements of the total OH* chemiluminescence were also conducted using a Hamamatsu H3695-10 PMT located approximately 6 cm away from the burner. A bandpass filter (center wavelength = 310 nm, FWHM = 10 nm) was placed in front of the PMT to reject interfering emissions. The current output of the PMT was converted to a voltage signal by a 10-k Ω resistor. The -3 dB bandwidth of the PMT measurements, as determined by both the transimpedance gain (10-k Ω) and the parasitic capacitance (160 pF) of the signal line, was approximately 100 kHz. This translates to an effective temporal resolution of $\tau_{1/e} = 1.6 \mu\text{s}$. The PMT signal of OH* chemiluminescence was recorded simultaneously with the MCT detector signal of transmitted laser intensity at a rate of 100 MS/s using a two-channel data acquisition module (National Instruments, PXI-5122).

2.2. Frequency analysis and phase-locked cycle averaging of chemiluminescence signal

For a pulsating flame, the frequency content of the total chemiluminescence signal was first analyzed using fast Fourier transform (FFT). The results were expressed in terms of normalized power spectral density (NPSD), as shown in Eqn. (1).

$$S(f_k) = \frac{1}{N\Delta f} \cdot \frac{|\sum_{i=1}^N I(t_i)e^{-2\pi j f_k t_i}|^2}{\sum_{i=1}^N I(t_i)^2} \quad (1)$$

In Eqn. (1), $f_k = k\Delta f$ denotes the k -th discrete Fourier frequency, with Δf being the reciprocal of the total measurement time $T = N\Delta t$ (1 s in the current study). $S(f_k)$ denotes the NPSD of the chemiluminescence signal evaluated at f_k . $I(t_i)$ represents the discrete-time chemiluminescence signal sampled at $t_i = i\Delta t$, and j denotes the imaginary unit. $S(f_k)$ is also expressed in logarithmic units (dB/Hz) as follows.

$$\hat{S}(f_k) = 10 \log_{10} S(f_k) \quad (2)$$

A harmonic power analysis method was employed to extract the fundamental frequency of oscillation, f_{osc} , by exploiting the fact that the frequency content of a periodic physical event consists of harmonics that are phase-locked, whereas the frequency content of noise or random fluctuations is uncorrelated. Specifically, f_{osc} was determined by solving a constrained optimization problem, namely maximizing the total power of harmonics within a search window $[f_{min}, f_{max}]$ estimated from the NPSD result, as shown below.

$$f_{osc} = \operatorname{argmax}_{[f_{min}, f_{max}]} \sum_{k=1}^M \left| \sum_{i=1}^N I(t_i)e^{-2\pi j k f t_i} \right|^2 \quad (3)$$

This optimization problem was solved numerically using a brute-force search algorithm, and to improve computational efficiency and robustness, the number of harmonics was truncated to $M = 5$. In the current study, this method was able to determine the primary oscillation frequency with a typical uncertainty of less than 0.1 Hz (defined by the frequency offset at 95% maximum total power), which was an order of magnitude better than the conventional FFT.

Once the primary oscillation frequency was determined, the chemiluminescence images of the pulsating flames were further analyzed using phase-locked cycle averaging. The recorded image sequence was divided into sub-sequences corresponding to individual cycles of oscillation, and images captured at the same relative time within each cycle were averaged across different sub-sequences. The starting frame of each sub-sequence was fine-tuned through cross-correlation analysis, using the spatially integrated chemiluminescence signal as a reference, which effectively removed random jitters in the oscillation cycles. This procedure was executed iteratively until convergence was achieved, usually within 2-3 iterations. This phase-locked cycle averaging successfully removed random fluctuations and revealed the underlying physical trends consistent across cycles, without degrading the effective temporal resolution of the current measurements (100 μs).

2.3. Axisymmetric reconstruction of temperature fields from laser absorption measurement

Spatially resolved measurements of local gas temperature were achieved by scanning the laser beams across the flame. An example measurement of a pulsating CH₄-O₂ flame at lower flow rates ($\dot{m}_{\text{CH}_4} = 0.20$ SLPM and $\dot{m}_{\text{O}_2} = 0.30$ SLPM, respectively) is illustrated in Fig. 2. Under the specific conditions of this measurement, the flame exhibited a regular mode of oscillation that was periodic in time and nearly axisymmetric in space, as confirmed by time-synchronized chemiluminescence imaging. For oscillating flames exhibiting axial symmetry, a reconstruction scheme using constrained optimization was developed to infer the spatial distribution of temperature from the absorbance data at different beam locations.

The line-of-sight absorbance $\alpha(t; y_i)$ was determined at each beam location y_i from the transmitted laser intensity $I(t; y_i)$ and a reference intensity profile $I_0(t)$ measured in the absence of absorption, based on the Beer-Lambert relation:

$$\alpha(t; y_i) = -\ln [I(t; y_i)/I_0(t)] \quad (4)$$

From the time sequence of $\alpha(t; y_i)$, an absorbance spectrum $\alpha(\nu; y_i)$ was obtained based on the laser wavenumber modulation profile $\nu(t)$ characterized prior to the flame experiment. A total of 12 absorption features in the spectral region of 2392.5 to 2397 cm^{-1} were analyzed, and the integrated absorbance over each selected transition feature (denoted by $[\nu_{k-}, \nu_{k+}]$) was

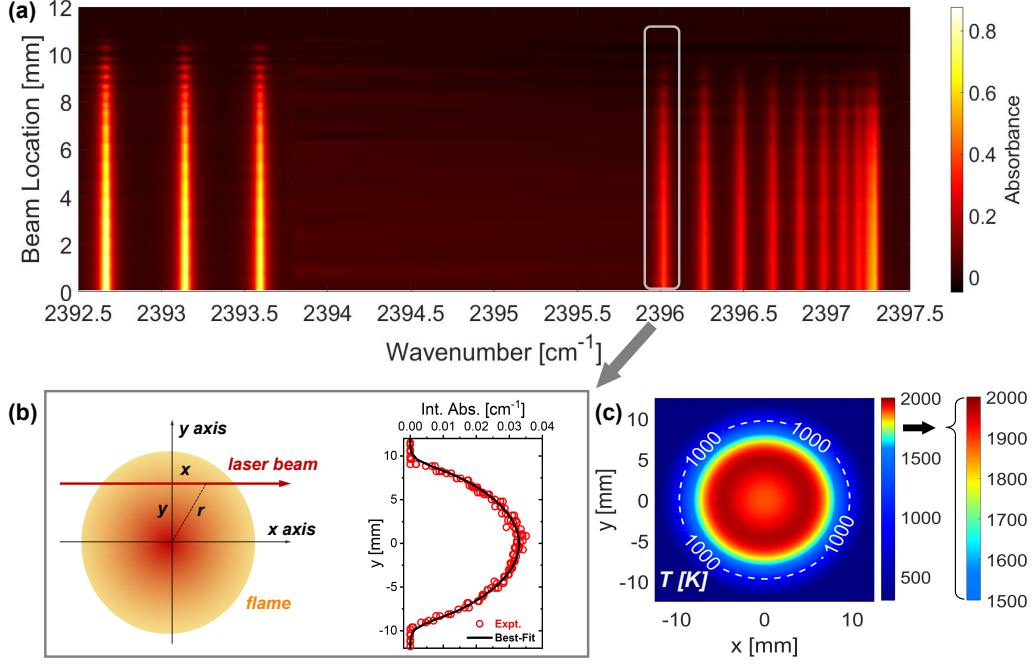


Figure 2: Example measurement of a premixed $\text{CH}_4\text{-O}_2$ flame pulsating in a single axisymmetric mode under the conditions of $\dot{m}_{\text{CH}_4} = 0.20$ SLPM and $\dot{m}_{\text{O}_2} = 0.30$ SLPM. (a) A spectrogram of the absorbance signal at different beam locations, with data obtained from various oscillation cycles at a fixed relative time of 10 ms. (b) The integrated absorbance of an isolated feature at different beam locations. (c) The Spatial distribution of gas temperature reconstructed from integrated absorbances under the assumption of axial symmetry.

used in the axisymmetric reconstruction, i.e.,

$$A_k(y_i) = \int_{\nu_{k-}}^{\nu_{k+}} \alpha(\nu; y_i) d\nu \quad (5)$$

To determine the spatial distribution of gas temperature, the entire spatial domain of interest was discretized using a number of sample points r_s along the radial direction. These sample points were selected based on the effective spatial resolution of the current laser diagnostic (1 mm, as defined by the laser beam diameter). At each sample point, a local gas temperature T_s and a CO_2 mole fraction X_s were assigned. The integrated absorbance of each

absorption feature was evaluated first at each sample point $A_k^0(r_s; T_s, X_s)$ and then summed along each line of sight (see Fig. 2(b)), yielding:

$$A_k^0(r_s; T_s, X_s) = P X_s S_k^0(T_s) \quad (6)$$

and

$$A_k(y_i) = \int_{-\infty}^{+\infty} A_k^0\left(\sqrt{x^2 + y_i^2}\right) dx \approx \sum_{s=1}^{\#pts.} w_{is} \cdot A_k^0(r_s; T_s, X_s) \quad (7)$$

In the above equations, a constant flame pressure of $P = 1$ atm was assumed, and the linestrength of each transition feature, S_k^0 , was calculated as a function of the local gas temperature from the HITEMP spectroscopy model [46]. The line-of-sight integration was numerically evaluated using Gauss–Legendre quadrature, with linear interpolation between sample points. This approach effectively approximated the integral as a weighted sum of the integrated absorbances at selected sample points. The weight factor w_{is} was a geometric constant independent of the laser wavenumber ν and the local gas properties T_s and X_s . The integrated absorbances were assembled into two column vectors of $\mathbf{A}^0(\mathbf{T}, \mathbf{X}) = \{A_k^0(r_s; T_s, X_s)\}$ and $\mathbf{A} = \{A_k(y_i)\}$, with \mathbf{T} and \mathbf{X} representing $\{T_i\}$ and $\{X_i\}$, respectively. All weight factors $\{w_{is}\}$ were compiled into a constant matrix \mathbf{W} . The optimal values of \mathbf{T} and \mathbf{X} were determined by solving the following nonlinear optimization problem:

$$(\mathbf{T}^*, \mathbf{X}^*) = \operatorname{argmin} \left\| \mathbf{A} - \mathbf{W} \mathbf{A}^0(\mathbf{T}, \mathbf{X}) \right\|_2^2 + \lambda_T^2 \|\mathbf{L}\mathbf{T}\|_2^2 + \lambda_X^2 \|\mathbf{L}\mathbf{X}\|_2^2 \quad (8)$$

The last two terms in Eqn. 8 represent smoothness regularization, with \mathbf{L} being the discrete Laplacian matrix and λ_T and λ_X serving as the regularization strength factors. The values of λ_T and λ_X were generally kept small to avoid blurring the reconstructed distributions, while being sufficiently large to ensure numerical stability and suppress random fluctuations; in the current study, they were set to 1×10^{-5} and 1×10^{-1} , respectively. Eqn. 8 was solved iteratively using the sequential quadratic programming method. The resulting spatial distributions of temperature and CO_2 mole fraction are shown in Fig. 4(c), with a typical measurement precision of 1%. Further discussion on the uncertainty analysis, as well as the choice of λ_T and λ_X , can be found in a recent work by the authors [44].

3. Results and Discussion

A total of 838 pulsating flame experiments were conducted at equivalence ratios (ϕ) ranging from 1.18 to 2.35 and dilution factors (η , defined as $\dot{m}_{CH_4}/(\dot{m}_{CH_4} + \dot{m}_{CO_2})$) ranging from 0.26 to 1.00. The primary frequencies, oscillation modes, regime diagrams, and fuel dependence of these pulsating flames are discussed as follows. A summary of the frequencies and modes of these oscillating flames can be found in Supplementary Material I.

3.1. Pulsation frequencies

The primary oscillation frequency (f_{osc}) of a pulsating flame was determined using the method described in Section 2.2. Across the range of the current experimental conditions, this frequency varied from 26.4 to 1866.0 Hz, exhibiting a negative dependence on the equivalence ratio and a positive dependence on the dilution factor.

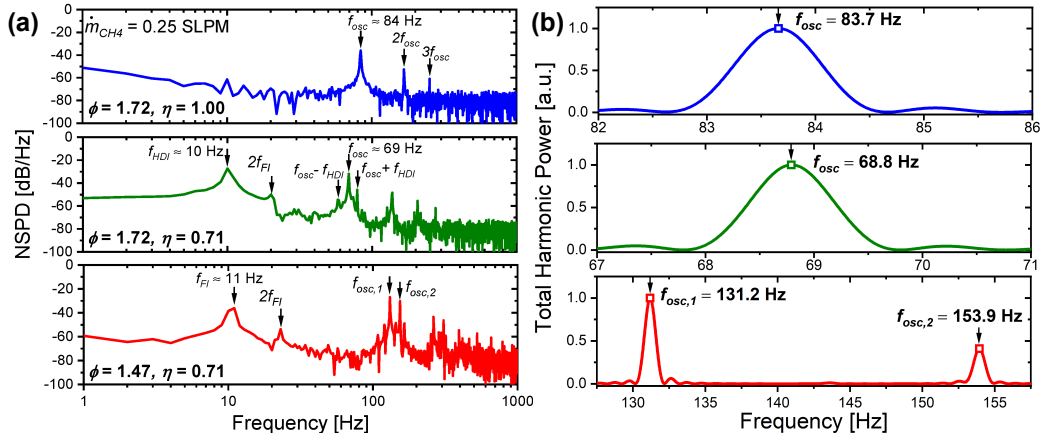


Figure 3: (a) Representative OH* NPSD spectra of pulsating flames at three different conditions. Top (blue): at $\phi = 1.72, \eta = 1.00$, the NPSD spectrum consists of equally spaced harmonics of a single fundamental frequency, indicating the presence of single-mode oscillation. Middle (green): at $\phi = 1.72, \eta = 0.71$, low-frequency flickering instability appears, which couples with the single-mode oscillation and creates sidebands around the harmonics. Bottom (red): at $\phi = 1.47, \eta = 0.71$, multiple fundamental oscillation frequencies (and their harmonics) are observed. f_{osc} : the primary oscillation frequency; f_{FI} : the flickering instability frequency. (b) Total harmonic power analysis of the three pulsating flames.

Some representative OH* NPSD spectra of pulsating flames are illustrated

in Fig. 3. Depending on the specific flow rates of fuel, O_2 , and CO_2 , the flame oscillations can exhibit distinctly different characteristics. The top panel of the figure presents a typical example of fuel-rich, undiluted (or weakly diluted), low-speed flames, where both the heat release rate and the mean flow velocity are relatively low. The NPSD spectrum contains equally spaced harmonics of a single fundamental frequency around 84 Hz, with no other frequency content observed. These characteristics indicate that the flame oscillates in a single periodic mode, as corroborated by the single peak in the total harmonic power spectrum displayed in the right panel.

At higher flow velocities, a second, low-frequency oscillation appeared around 10 Hz and created sidebands around the primary oscillation frequency, as shown in the middle panel of the figure. Across the experimental conditions explored in the current study, the frequency of this second oscillation was found to be relatively stable (9 - 12 Hz) and largely independent of the equivalence ratio and dilution level, suggesting that it must have originated from a mechanism different from the high-frequency thermo-diffusive pulsation.

To further investigate the nature of this low-frequency oscillation, additional experiments were conducted using a CMOS camera to monitor the chemiluminescence signal of an undiluted, moderately fuel-rich flame from the side, as illustrated in Fig. 4. Under these conditions, the flame did not exhibit any high-frequency pulsation; only a low-frequency oscillation at a fundamental frequency of 11 Hz was observed. The results indicate that the low-frequency component corresponds to flickering-type flame dynamics that is distinctively different from flame front pulsation. For example, throughout a flame flickering cycle, the base of the flame remained largely stationary, whereas the tail of hot burnt gas downstream of the flame exhibited an oscillating motion of elongation and contraction along the axial direction.

It turns out that the current observation of this rich premixed flame agrees well with classic studies on diffusion flames, in terms of both the overall phenomenon and the range of oscillation frequencies (e.g., [47, 48]). According to these studies, such low-frequency oscillations of the flame result from buoyancy-induced flow surrounding the flame. The velocity difference between the hot burnt gases and the cold ambient air creates an unstable shear layer, which rolls up into toroidal vortices and sheds periodically. The current study thus refers to this low-frequency oscillation as the flame flickering instability, with its frequency denoted as f_{FI} .

At higher heat release rates (i.e., higher fuel flow rates and/or lower equiv-

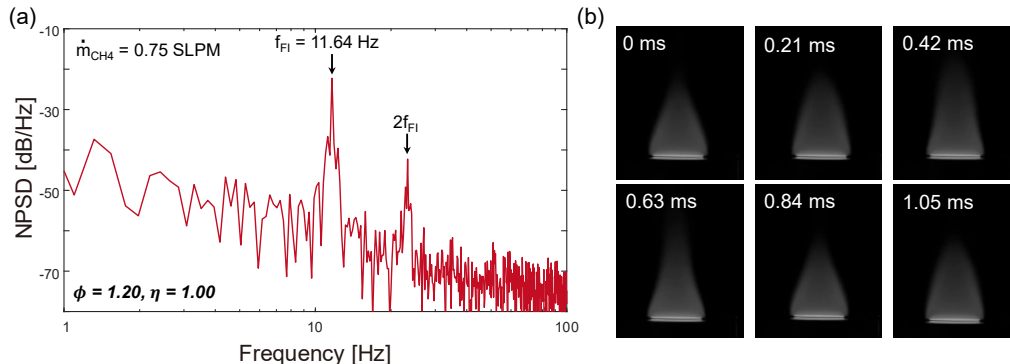


Figure 4: representative example on the low-frequency oscillation of a methane-oxygen flame at $\phi = 1.20$, $\eta = 1.00$. (a) the FFT spectrum of CH^* normalized power spectral density (NPSD), (b) sequential side-view images of the flame.

alence ratios), the sidebands around the primary oscillation frequency of the flame further split into two or more fundamental oscillation frequencies, each accompanied by its own harmonics, as shown in the bottom panel of Fig. 3. In the current study, this phenomenon is termed multi-mode oscillation. In this context, the corresponding primary oscillation frequency is defined as the fundamental frequency of the stronger mode. Three representative cases of different flame oscillation modes have been selected for further analysis, as discussed in the next section.

3.2. Single-mode oscillation

Fig. 5 presents the dynamic evolution of multiple scalar fields in a single-mode pulsating flame under the conditions of $\dot{m}_{\text{CH}_4} = 0.20$ SLPM and $\dot{m}_{\text{O}_2} = 0.30$ SLPM. The top panel of the figure illustrates the temporal evolution of chemiluminescence signal in a cycle, where phase-locked averaging was applied to remove random fluctuations and increase the signal-to-noise ratio. The resulting data has been normalized to a relative intensity scale of -1 to 1. Excellent agreement is seen between the pixel-integrated signal of chemiluminescence image and the PMT signal. Within each oscillation cycle of approximately 65 ms, the total chemiluminescence is seen to increase during the first 45 ms and decrease during the last 20 ms.

Eight representative frames of the cycle-averaged chemiluminescence images are shown in Fig. 5(b) in pseudocolors, with red and blue representing high and low chemiluminescence signals, respectively. The mean intensity has

been subtracted from each pixel to enhance contrast and highlight dynamic changes. From these images, the pulsating flame is observed to oscillate in a propagating ring mode, with concentric waves of local heat release rate perturbation originating from the edge and traveling toward the flame center, where they merge and terminate before the next oscillation cycle.

It is worth noting that, although the measured images were line-of-sight integrated, no significant cancellation effect was expected in the top-view images because the flame front remained close to a geometrically thin sheet throughout the oscillation cycle. Besides, the flame motion occurred primarily in the vertical direction, as revealed by additional side-view measurement of a single-mode pulsating flame shown in Fig. 6.

Fig. 5(c) illustrates the dynamic evolution of temperature distribution at a height above the burner (HAB) of 2.5 mm. A similar ring-type oscillation can be observed in the temperature distribution, but with a phase lag compared to the chemiluminescence signal. At the specific conditions of this experiment, the maximum local temperature is found to be approximately 2000 K, significantly lower than the adiabatic flame temperature (≈ 3000 K) due to heat loss at the water-cooled burner surface.

Fig. 5(d) shows the evolution of line-of-sight-averaged temperature within one oscillation cycle. In the current study, a high level of measurement precision (on the order of ± 5 K) has been achieved through cycle averaging, thereby allowing small variations to be discerned. The average temperature is seen to oscillate between 1760 and 1790 K, with a phase lag of 100 - 150 degrees relative to the chemiluminescence signal. The overall $1-\sigma$ uncertainties in these measurements are estimated to be 2 %, based on the uncertainty contributions from the spectral fitting (less than 0.1%), spectroscopy model (less than 1%), and small fluctuations in the laser intensity baseline (less than 1%).

Fig. 5(e) presents the vertical distribution of average temperature along the burner diameter, measured at different heights above the burner (HAB) and at various times during a single oscillation cycle. Its dynamic evolution reveals an interesting phenomenon that cannot be captured by the chemiluminescence imaging alone, namely, the existence of higher and lower average temperature regions and their vertical motion with time, which implies alternating puffs of hot and cool gas traveling in the vertical direction. Further investigation into the 2D/3D structure of the traveling flame fronts, especially in conjunction with velocity field measurement, may warrant future studies.

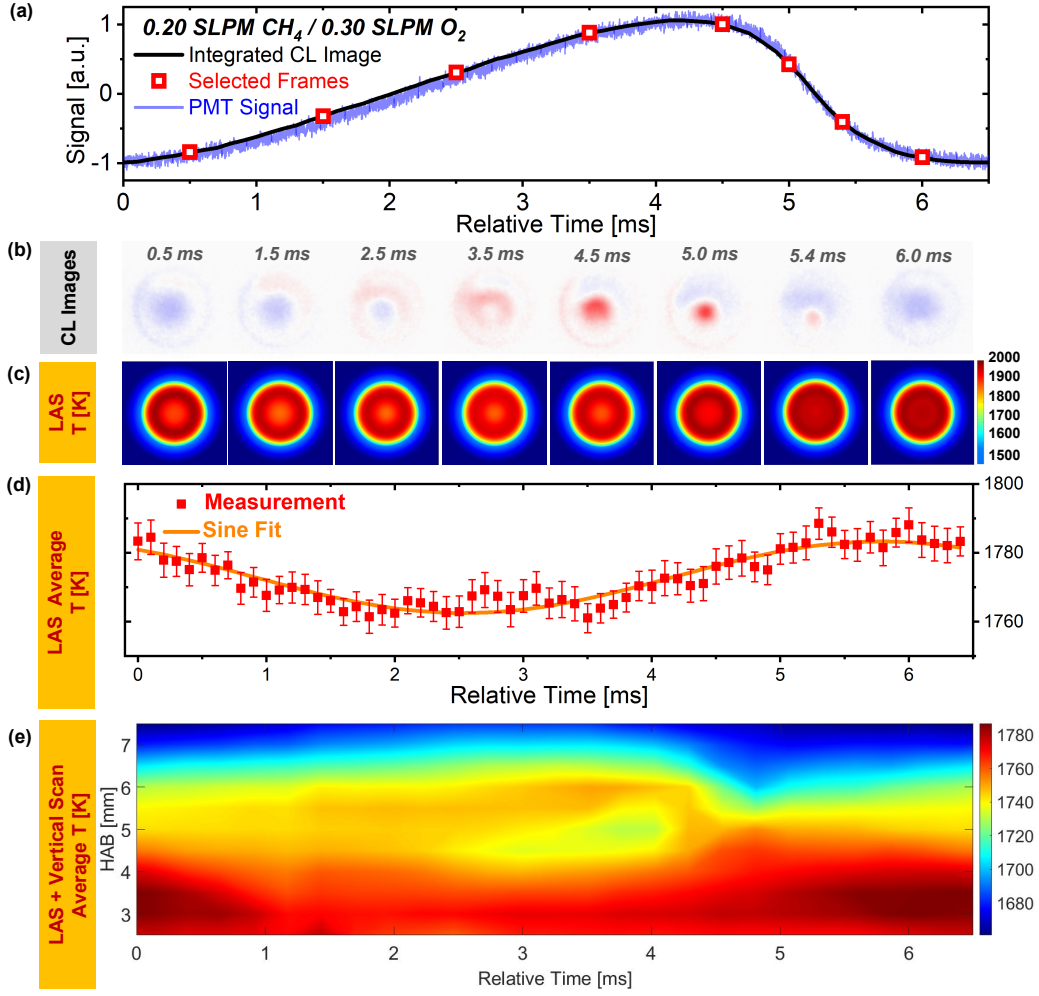


Figure 5: Spatiotemporally resolved measurements of a single-mode pulsating flame ($\phi = 1.33$, $\eta = 1.00$) at different times in the oscillation cycle. (a) Spatially integrated chemiluminescence signals from the high-speed camera (black) and the PMT (blue), normalized and phase-locked averaged over 90 cycles. (b) Phase-locked averaged chemiluminescence images. (c) Dynamic evolution of the gas temperature distribution at HAB = 2.5 mm. (d) Evolution of the average temperature along the burner diameter. Error bars denote the standard deviation of the measurements. (e) Evolution of the vertical distribution of average gas temperature along the burner diameter within a single oscillation cycle.

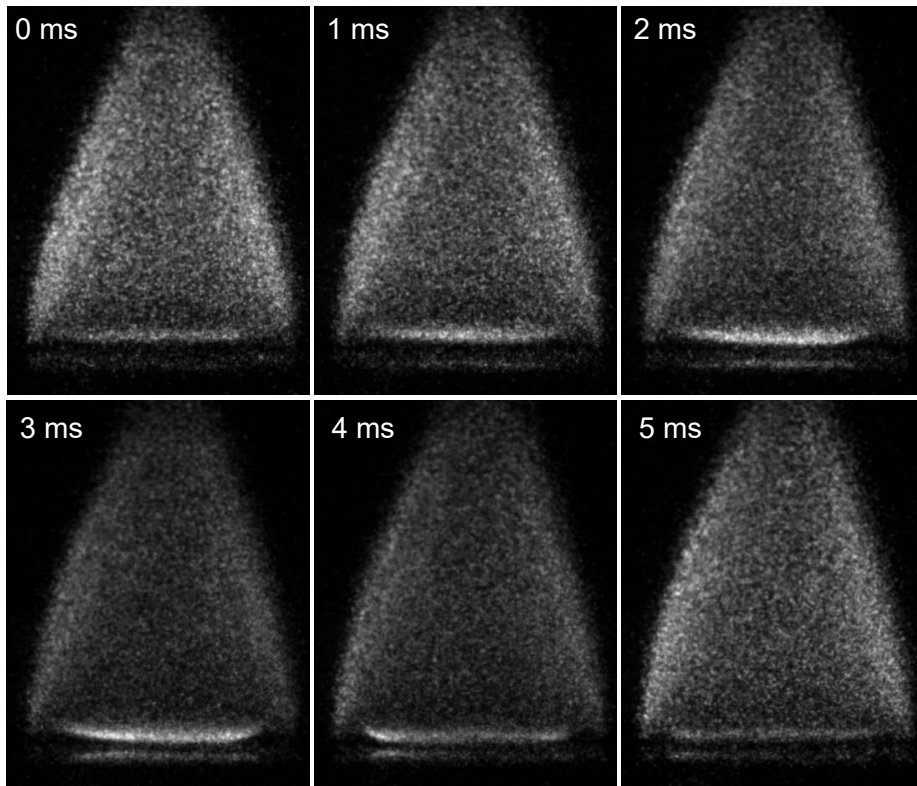


Figure 6: Side-view chemiluminescence images of a single-mode pulsating flame at $\phi = 2.00$, $\eta = 1.00$.

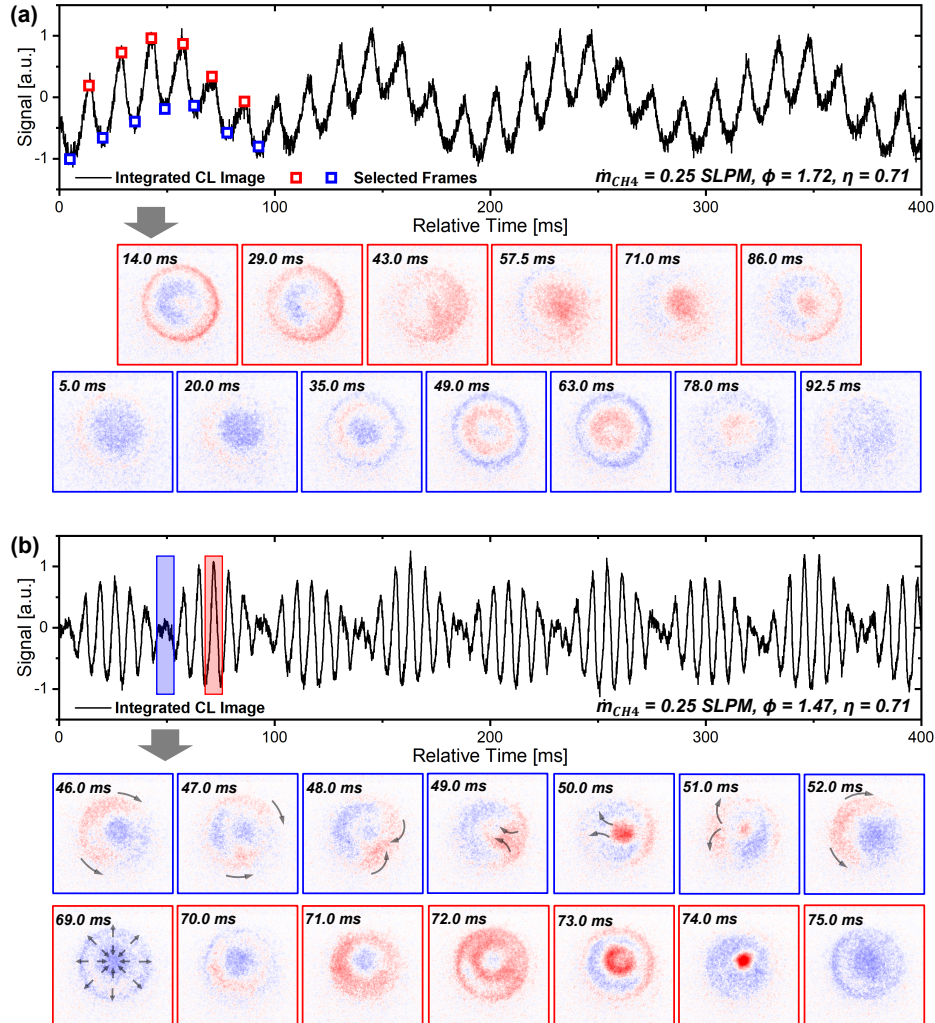


Figure 7: Chemiluminescence signal illustrating the spatiotemporal modes of flame oscillation. Selected frames of the cycle-averaged chemiluminescence images, after the subtraction of mean intensity, are presented in pseudocolors, with red and blue representing high and low signals, respectively. (a) Single-mode oscillation influenced by flickering instabilities at $\phi = 1.72$, $\eta = 0.71$. The dominant flame oscillation mode appears to be a fast centripetal traveling wave that is nearly axisymmetric. The flickering instabilities are manifested as a slow edge-mode perturbation that modulates the relative phase of the fast flame oscillation without significantly affecting its amplitude and spatial distribution. (b) Multi-mode oscillation at $\phi = 1.47$, $\eta = 0.71$. The integrated chemiluminescence intensity exhibits a clear beat pattern, indicating the presence of two fundamental oscillation frequencies that interfere with each other. The propagation directions and spatial patterns of flame oscillations during periods of constructive and destructive interference are drastically different.

3.3. Multi-mode oscillation

Two more complex cases of pulsating flames are presented in Fig. 7, including: (a) single-mode oscillations coupled with flickering instabilities, and (b) multi-mode oscillations. In the former case, the dominant flame oscillation mode remains a centripetal traveling wave, but flickering instabilities introduce a slow edge-mode perturbation that modulates its relative phase without significantly affecting its amplitude and spatial distribution. In the latter case, the amplitude of the flame oscillation varies significantly over time.

For example, in a representative measurement shown in Fig. 7(b), the integrated chemiluminescence intensity exhibits a clear beat pattern, indicating the presence of two fundamental oscillation frequencies interfering with each other. During the time interval of constructive interference, the spatial pattern of the flame oscillation remains axisymmetric, while the propagation of the heat release rate perturbation becomes bidirectional – waves originate from a ring zone and travel toward both the center and the edge of the burner. In contrast, during the time interval of destructive interference, the flame oscillation pattern appears drastically different: perturbation waves travel along two separate loops near the top and bottom edges of the burner and meet along the diameter. More complex interactions among three or more modes have also been observed at much higher heat release rates.

Dynamic Mode Decomposition (DMD) analysis was also performed on selected OH* image sequences, which yielded primary frequencies that agreed well with the previous results (within ± 1 Hz, see Supplementary Material II for further details). Note, however, that the DMD analysis should be regarded as a mathematical tool that seeks the optimal approximation to the measurement data but does not always guarantee physically meaningful results, as it can be prone to various forms of experimental uncertainties. In contrast, the current study primarily relied on the phase-locked method (as described in Section 2.2) for cycle-averaged analysis.

3.4. Regime diagrams

The primary frequencies and modes of pulsating CH₄-O₂-CO₂ flames, measured under various fuel flow rates, equivalence ratios, and dilution factors, are provided in Supplementary Material I. These results are also summarized in regime diagrams and frequency contour plots, as displayed in Figs. 8 and 9. Under the current experimental configuration, pulsating flame instability was observed only under fuel-rich conditions, specifically within the

equivalence ratio range of 1.18 to 2.50. The range of unstable equivalence ratios narrows with increasing CO₂ dilution (decreasing η), while its dependence on the CH₄ flow rate is non-monotonic – first expanding with increasing CH₄ flow rate, then peaking around 0.4 SLPM, and finally shrinking to a single point. This trend is consistent with the results reported previously in [27]. The highest CH₄ flow rate at which flame pulsation was observed occurs near 1.32 SLPM, with the corresponding equivalence ratio and dilution factor being $\phi = 1.48$ and $\eta = 1.00$, respectively.

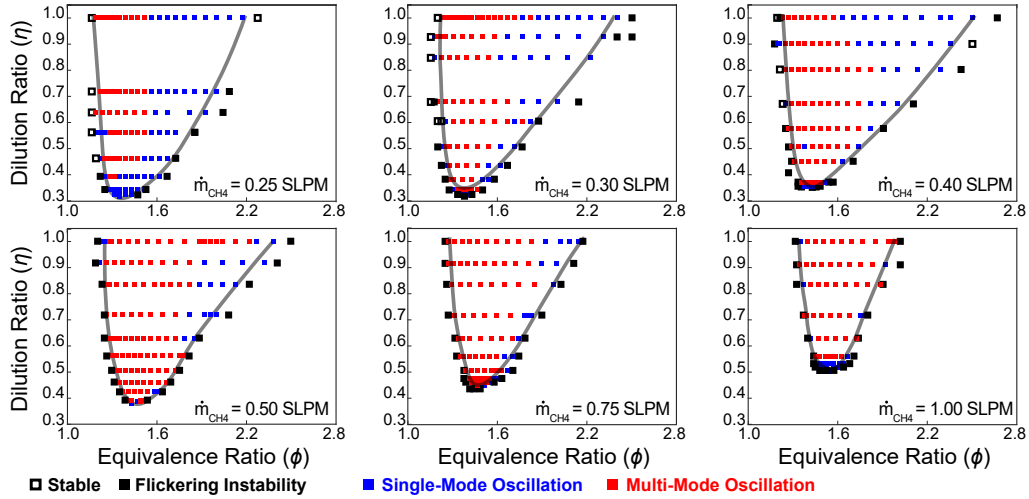


Figure 8: Regime diagrams of instability modes at selected CH₄ mass flow rates. Lines indicate the observed stability boundaries.

The single-mode oscillation regimes are generally narrower than those of multi-mode oscillations, except at low CH₄ flow rates (0.25 SLPM or less), where heat losses to the burner are significant. At CH₄ flow rates of 0.5 SLPM or higher, the single-mode regimes are confined to the vicinity of stability boundaries. The primary oscillation frequency is observed to increase with the mass flow rate of CH₄ and decrease with the equivalence ratio, exhibiting a strong correlation with the flame’s thermal power. In contrast, the influence of the CO₂ dilution factor on the primary oscillation frequency is less significant.

Another interesting observation is that the transition between single-mode and multi-mode oscillations is almost always accompanied by flickering instabilities. A close examination of the NPSD spectra (Fig. 3, where the difference between $f_{osc,1}$ and $f_{osc,2}$ is close to $2f_{FI}$) and the chemiluminescence

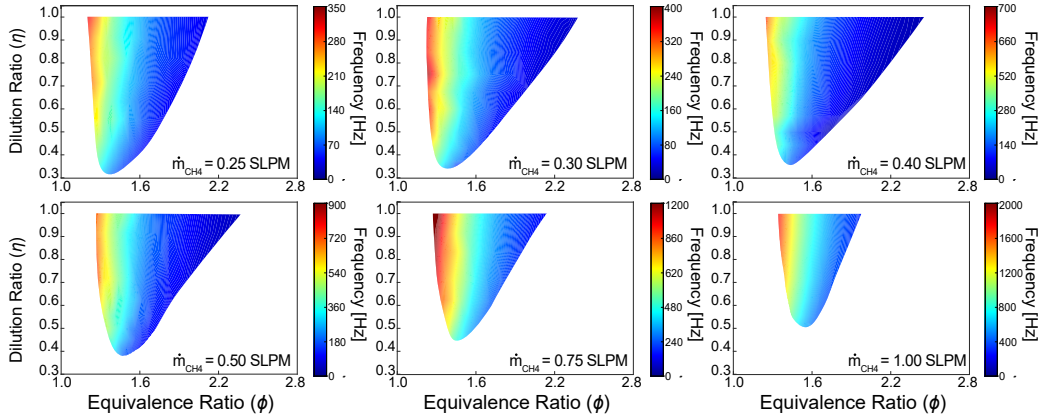


Figure 9: Parametric dependence of the primary oscillation frequency of a pulsating $\text{CH}_4\text{-O}_2\text{-CO}_2$ flame.

images (Fig. 7, where the edge mode plays an important role) suggests that the multi-mode oscillations are likely triggered by these flickering instabilities through nonlinear interactions. Further investigation into the transient dynamics of mode transition and the effects of flickering instabilities is currently in progress, particularly under microgravity conditions to eliminate the interference of buoyancy effects.

4. Conclusions

The pulsating instabilities of premixed $\text{CH}_4\text{-O}_2$ flames on a porous-plug burner were investigated at various levels of CO_2 dilution, across a wide range of equivalence ratios, and flow rates. Time-resolved measurements of flame chemiluminescence and average temperature were obtained, from which the primary oscillation frequencies of the pulsating flames were determined using fast Fourier transform and harmonic power analysis. Additionally, spatiotemporally resolved measurements of gas temperature were conducted using spectrally modulated laser absorption diagnostics synchronized with high-speed chemiluminescence imaging.

From the results of the current measurements, a mode transition phenomenon in the pulsating flames was revealed through phase-locked analysis. Under fuel-rich conditions with relatively low heat release rates and flow rates, the flames exhibited quasi-periodic pulsation in a single mode. At elevated flow rates, flickering instability appeared and began to interfere

with the thermo-diffusive pulsation, creating sidebands around the primary frequency. As the heat release rate increased, mode splitting occurred, and the flames eventually pulsated in multiple modes. The stability boundaries and regime diagrams of the flame oscillation modes were obtained, and representative examples of different modes were analyzed.

Although obtained from experiments on a specific porous-plug burner, the results of the current study – such as the overall trends of the stability boundary, primary frequency, and mode distributions – are expected to be broadly applicable to other CO₂-diluted oxy-fuel combustion systems. They provide a basis for theoretical and numerical extrapolation toward applications relevant to practical combustion devices, where flame stability is a critical design consideration. While the current study primarily focused on methane flames, the underlying concepts can be easily extended to other fuels such as hydrogen and ammonia. In this sense, the present study should prove valuable for both fundamental research on flame dynamics and practical applications of CO₂-moderated oxy-combustion.

Acknowledgments

This research is supported by the National Natural Science Foundation of China under Grants No. 92152108 and No. 12472278, and the Space Application System of China Manned Space Program under projects "Nonlinear Dynamics of Flame Instability under Microgravity Conditions" and "Ignition Mechanism of Premixed Near-Limit Flames under Microgravity Conditions".

Supplementary Material

Supplementary Material I: Data summary of flame oscillation frequencies and modes under conditions explored in the current study. Supplementary Material II: Representative results of dynamic mode decomposition analysis.

References

- [1] S. Candel, Combustion dynamics and control: Progress and challenges, Proceedings of the Combustion Institute 29 (2002) 1–28.
- [2] T. Poinsot, Prediction and control of combustion instabilities in real engines, Proceedings of the Combustion Institute 36 (2017) 1–28.

- [3] T. C. Lieuwen, *Unsteady combustor physics*, Cambridge University Press, 2021.
- [4] H. Pitsch, The transition to sustainable combustion: Hydrogen-and carbon-based future fuels and methods for dealing with their challenges, *Proceedings of the Combustion Institute* 40 (2024) 105638.
- [5] Z. Abubakar, E. M. Mokheimer, M. M. Kamal, A review on combustion instabilities in energy generating devices utilizing oxyfuel combustion, *International Journal of Energy Research* 45 (2021) 17461–17479.
- [6] M. Matalon, Intrinsic flame instabilities in premixed and nonpremixed combustion, *Annual Review of Fluid Mechanics* 39 (2007) 163–191.
- [7] G. Sivashinsky, Instabilities, pattern formation, and turbulence in flames, *Annual Review of Fluid Mechanics* 15 (1983) 179–199.
- [8] J. Buckmaster, The structure and stability of laminar flames, *Annual Review of Fluid Mechanics* 25 (1993) 01–34.
- [9] P. Clavin, Premixed combustion and gasdynamics, *Annual Review of Fluid Mechanics* 26 (1994) 321–352.
- [10] C. K. Law, G. Jomaas, J. K. Bechtold, Cellular instabilities of expanding hydrogen/propane spherical flames at elevated pressures: theory and experiment, *Proceedings of the Combustion Institute* 30 (2005) 159–167.
- [11] S. Kadowaki, H. Suzuki, H. Kobayashi, The unstable behavior of cellular premixed flames induced by intrinsic instability, *Proceedings of the Combustion Institute* 30 (2005) 169–176.
- [12] J. Yu, R. Yu, X. Fan, M. Christensen, A. Konnov, X.-S. Bai, Onset of cellular flame instability in adiabatic $\text{CH}_4/\text{O}_2/\text{CO}_2$ and CH_4/air laminar premixed flames stabilized on a flat-flame burner, *Combustion and Flame* 160 (2013) 1276–1286.
- [13] W. Jin, J. Wang, S. Yu, Y. Nie, Y. Xie, Z. Huang, Cellular instabilities of non-adiabatic laminar flat methane/hydrogen oxy-fuel flames highly diluted with CO_2 , *Fuel* 143 (2015) 38–46.

- [14] D. Lapalme, F. Halter, C. Mounaïm-Rousselle, P. Seers, Characterization of thermodiffusive and hydrodynamic mechanisms on the cellular instability of syngas fuel blended with CH₄ or CO₂, *Combustion and Flame* 193 (2018) 481–490.
- [15] H. J. Kim, K. Van, D. K. Lee, C. S. Yoo, J. Park, S. H. Chung, Laminar flame speed, markstein length, and cellular instability for spherically propagating methane/ethylene–air premixed flames, *Combustion and Flame* 214 (2020) 464–474.
- [16] L. Jiang, C. Gu, G. Zhou, F. Li, Q. Wang, Cellular instabilities of n-butane/air flat flames probing by PLIF-OH and PLIF-CH₂O laser diagnosis, *Experimental Thermal and Fluid Science* 118 (2020) 110155.
- [17] E. Antar, J. Delavande, E. Robert, Experimental characterization of diffusive-thermal instabilities in CO₂-diluted H₂-CH₄-CO unstrained diffusion flames, *Combustion and Flame* 250 (2023) 112636.
- [18] T. Zirwes, F. Zhang, T. L. Kaiser, K. Oberleithner, O. T. Stein, H. Bockhorn, A. Kronenburg, The role of thermodiffusion and dimensionality in the formation of cellular instabilities in hydrogen flames, *Proceedings of the Combustion Institute* 40 (2024) 105665.
- [19] G. Sivashinsky, Diffusional-thermal theory of cellular flames, *Combustion Science and Technology* 15 (1977) 137–145.
- [20] V. Mislavskii, N. Pestovskii, S. Tskhai, B. Kichatov, V. Gubernov, V. Bykov, U. Maas, Diffusive-thermal pulsations of burner stabilized methane-air flames, *Combustion and Flame* 234 (2021) 111638.
- [21] V. Gubernov, V. Bykov, U. Maas, Hydrogen/air burner-stabilized flames at elevated pressures, *Combustion and Flame* 185 (2017) 44–52.
- [22] E. Christiansen, C. Law, C. Sung, Steady and pulsating propagation and extinction of rich hydrogen/air flames at elevated pressures, *Combustion and Flame* 124 (2001) 35–49.
- [23] C. Sung, A. Makino, C. Law, On stretch-affected pulsating instability in rich hydrogen/air flames: asymptotic analysis and computation, *Combustion and Flame* 128 (2002) 422–434.

- [24] J. Yuan, Y. Ju, C. K. Law, Pulsating and hydrodynamic instabilities at large lewis numbers, *Combustion and Flame* 144 (2006) 386–397.
- [25] Y.-C. Wu, Z. Chen, Asymptotic analysis of outwardly propagating spherical flames, *Acta Mechanica Sinica* 28 (2012) 359–366.
- [26] Y. Cai, T. Li, M. Du, J. Li, Effects of thermodiffusive instability on the spherical premixed flames anchored to a porous-plug burner, *Aerospace Science and Technology* 97 (2020) 105632.
- [27] V. N. Kurdyumov, M. Matalon, The porous-plug burner: Flame stabilization, onset of oscillation, and restabilization, *Combustion and Flame* 153 (2008) 105–118.
- [28] V. N. Kurdyumov, M. Sánchez-Sanz, Influence of radiation losses on the stability of premixed flames on a porous-plug burner, *Proceedings of the Combustion Institute* 34 (2013) 989–996.
- [29] S. B. Margolis, Effects of selective diffusion on the stability of burner-stabilized premixed flames, *Symposium (International) on Combustion* 18 (1981) 679–693.
- [30] J. Blackshear Jr, J. Mapp, M. Gorman, An experimental study of pulsating low pressure flames, *Combustion Science and Technology* 35 (1984) 311–315.
- [31] H. Pearlman, Target and spiral wave patterns in premixed gascombustion, *Journal of the Chemical Society, Faraday Transactions* 93 (1997) 2487–2490.
- [32] S. Nechipurenko, T. Miroshnichenko, N. Pestovskii, S. Tskhai, B. Kichatov, V. Gubernov, V. Bykov, U. Maas, Experimental observation of diffusive-thermal oscillations of burner stabilized methane-air flames, *Combustion and Flame* 213 (2020) 202–210.
- [33] A. Moroshkina, V. Mislavskii, B. Kichatov, V. Gubernov, V. Bykov, U. Maas, Burner stabilized flames: Towards reliable experiments and modelling of transient combustion, *Fuel* 332 (2023) 125754.

- [34] A. Moroshkina, E. Yakupov, V. Mislavskii, E. Sereshchenko, A. Polezhaev, S. Minaev, V. Gubernov, V. Bykov, The performance of reaction mechanism in prediction of the characteristics of the diffusive-thermal oscillatory instability of methane–hydrogen–air burner-stabilized flames, *Acta Astronautica* 215 (2024) 496–504.
- [35] D. Volkov, A. Moroshkina, V. Mislavskii, E. Sereshchenko, V. Gubernov, V. Bykov, S. Minaev, Relaxational oscillations of burner-stabilized premixed methane–air flames, *Combustion and Flame* 259 (2024) 113141.
- [36] N. Li, V. Bykov, A. Moroshkina, E. Sereshchenko, V. Gubernov, Two dimensional flame structure of oscillating burner-stabilized methane-air flames, *Combustion and Flame* 276 (2025) 114115.
- [37] T. Neill, D. Judd, E. Veith, D. Rousar, Practical uses of liquid methane in rocket engine applications, *Acta Astronautica* 65 (2009) 696–705.
- [38] S. Boulal, N. Fdida, L. Matuszewski, L. Vingert, M. Martin-Benito, Flame dynamics of a subscale rocket combustor operating with gaseous methane and gaseous, subcritical or transcritical oxygen, *Combustion and Flame* 242 (2022) 112179.
- [39] D. Singh, E. Croiset, P. L. Douglas, M. A. Douglas, Techno-economic study of co₂ capture from an existing coal-fired power plant: Mea scrubbing vs. o₂/co₂ recycle combustion, *Energy Conversion and Management* 44 (2003) 3073–3091.
- [40] R. Stanger, T. Wall, R. Spörl, M. Paneru, S. Grathwohl, M. Weidmann, G. Scheffknecht, D. McDonald, K. Myöhänen, J. Ritvanen, et al., Oxy-fuel combustion for CO₂ capture in power plants, *International Journal of Greenhouse Gas Control* 40 (2015) 55–125.
- [41] K. Andersson, F. Johnsson, Flame and radiation characteristics of gas-fired O₂/CO₂ combustion, *Fuel* 86 (2007) 656–668.
- [42] P. Heil, D. Toporov, M. Förster, R. Kneer, Experimental investigation on the effect of O₂ and CO₂ on burning rates during oxyfuel combustion of methane, *Proceedings of the Combustion Institute* 33 (2011) 3407–3413.

- [43] H. Kobayashi, H. Hagiwara, H. Kaneko, Y. Ogami, Effects of co2 dilution on turbulent premixed flames at high pressure and high temperature, *Proceedings of the Combustion Institute* 31 (2007) 1451–1458.
- [44] S. Zhang, S. Wang, Precision thermometry of flat flames using spatially resolved multi-color laser absorption spectroscopy of carbon dioxide, *Under Review* (2025). doi:<https://doi.org/10.48550/arXiv.2507.10064>.
- [45] H. Wang, Z. Yan, Y. Zhao, S. Wang, On the self-excited instabilities of premixed swirl flames near blow-off limits—an experimental study using simultaneous measurements of thermal boundary conditions and core flow scalar fields, *Combustion and Flame* 277 (2025) 114171.
- [46] L. S. Rothman, I. Gordon, R. Barber, H. Dothe, R. R. Gamache, A. Goldman, V. Perevalov, S. Tashkun, J. Tennyson, Hitemp, the high-temperature molecular spectroscopic database, *Journal of Quantitative Spectroscopy and Radiative Transfer* 111 (2010) 2139–2150.
- [47] J. Buckmaster, N. Peters, The infinite candle and its stability—a paradigm for flickering diffusion flames, *Symposium (International) on Combustion* 21 (1988) 1829–1836.
- [48] L.-D. Chen, J. Seaba, W. Roquemore, L. Goss, Buoyant diffusion flames, *Symposium (International) on Combustion* 22 (1989) 677–684.